AIAA JOURNAL
Vol. 42, No. 11, November 2004

Computational Analysis of an Independent Ramjet Stream in a Combined Cycle Engine

Ryan B. Bond*
Sandia National Laboratories, Albuquerque, New Mexico 87185
and
Jack R. Edwards†
North Carolina State University, Raleigh, North Carolina 27695

A new concept for the low-speed propulsion mode in rocket-based combined cycle engines has been developed as part of the NASA GTX program. This concept, called the independent ramjet stream (IRS) cycle, is a variation of the traditional ejector ramjet (ER) design and involves the injection of hydrogen fuel directly into the airstream, where it is ignited by the rocket plume. The advantage of the IRS design is that it allows for a single large rocket instead of several smaller rockets, and its required combustor length is smaller than that of a traditional ER design. Both of these features make the IRS design lighter. Experiments and computational fluid dynamics are currently being used to evaluate the feasibility of the new design. In this work, a Navier–Stokes code valid for general reactive flows is applied to the model engine under cold-flow, ER, and IRS cycle operation. Pressure distributions corresponding to cold-flow and ER operation are compared with experimental data. The engine response under IRS cycle operation is examined for different reaction models and grid sizes. The solutions exhibit a high sensitivity to both grid resolution and reaction mechanism but do indicate that thermal throat ramjet operation is possible through the injection and burning of additional fuel into the airstream.

Nomenclature

c	=	molar density
k	=	turbulence kinetic energy
M	=	Mach number, molar mass
MR	=	mass ratio
$\dot{m}$	=	mass flow rate, lbm/s (kg/s)
p	=	pressure, psia (kPa)
T	=	temperature, °R
x, y, z	=	Cartesian body axes, in. (cm)
Y	=	mass fraction
ε	=	dissipation per unit mass
ρ	=	density
ϕ	=	equivalence ratio
ω	=	specific dissipation rate

Subscripts

c	=	chamber
e	=	exit
i	=	inlet
t	=	total

Introduction

THE NASA GTX concept vehicle is a single-stage-to-orbit (SSTO) design that has incorporated rocket-based combined cycle (RBCC) engines. The GTX is one of several designs intended to demonstrate SSTO capability and evaluate RBCC technology.

The RBCC engines incorporated on the GTX are intended to operate in four modes. The first mode, used from liftoff to Mach 2.5, is the independent ramjet stream (IRS) cycle. In the IRS mode, hydrogen fuel is injected into the inlet diffuser section, where it mixes with the incoming air. This fuel–airstream then meets the rocket exhaust in the combustor section. The rocket motor provides thrust and acts as an ignition source for the fuel–air mixture. The rocket motor is typically run fuel rich, although not as rich as a conventional ejector ramjet (ER) design, in which no fuel injection occurs. In a conventional ER design, all of the fuel for the ramjet stream is contained within the rocket exhaust. Figure 1 shows a schematic of the engine design operating in IRS mode. The rocket plume is referred to as the "primary" stream, and the fuel–air mixture entering the combustor section via the isolator is referred to as the "secondary" stream. At lower inlet mass flow rates, the majority of the engine mass flow is contained within the primary stream, but as the vehicle accelerates, the secondary stream eventually becomes more significant than the primary stream.

A key requirement for the IRS concept is the ability to establish thermal-throat ramjet operation in the secondary stream within the allowable combustor length. In a thermal-throat ramjet, choking is achieved through the addition of heat rather than through a converging section with a minimum area sufficient to choke the flow. In this way, a diverging combustor section effectively behaves like a converging–diverging nozzle. If the heat release is high enough in the flame to overcome the effect of area change, then subsonic flow accelerates as if it is going through a converging section. Sufficient heat release will accelerate the flow to sonic and create a thermal throat. Downstream of the flame, where there is little or no heat release, the diverging effect of the geometry dominates, and the flow is accelerated supersonically.

As the launch vehicle gains speed and altitude, the rocket motor produces a smaller percentage of thrust, and its piloting capability becomes unnecessary. The rocket is gradually throttled back until, at around Mach 2.5, the rocket motor is shut off completely. This point is the transition from mode 1 to mode 2, which is a pure ramjet mode. This ramjet mode remains efficient until around Mach 6, when supersonic combustion becomes more practical. The transition from ramjet to scramjet is induced by a centerbody translation. This change in the inlet geometry allows for fully supersonic flow throughout the combustor. At around Mach 11, it is necessary to turn the rocket motor back on to maintain thrust. The centerbody is then translated again to close the inlet completely. The rocket provides

Received 8 August 2003; revision received 26 April 2004; accepted for publication 3 May 2004.

*Senior Member of Technical Staff, P.O. Box 5800, Mail Stop 0825; rbbond@sandia.gov. Member AIAA.

†Associate Professor, Department of Mechanical and Aerospace Engineering, Campus Box 7910; jredward@eos.ncsu.edu. Senior Member AIAA.

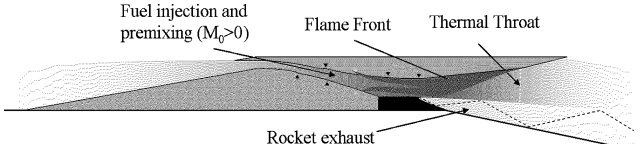

Fig. 1 Schematic of RBCC engine during IRS operation.

all of the thrust for the remainder of the ascent. More details about the GTX propulsion system's operation are given by Trefny.[1]

The IRS cycle is expected to have several advantages over the conventional ER cycle. ER designs typically require long combustor sections to allow for mixing of the fuel-rich rocket exhaust with the incoming air, burning, and establishment of a thermal throat. The IRS cycle could potentially allow for a shorter combustor section because much of the fuel would be premixed with the incoming airstream. Burning in premixed or partially premixed mode can result in flame propagation across the extent of the combustor and more rapid heat release.[2] Most ER designs employ multiple small rockets to enhance mixing, but the IRS design is more structurally efficient because it allows for a single large rocket. The IRS cycle is also expected to allow better transition into pure ramjet mode because fewer changes in the engine flowpath would be necessary for IRS-to-ramjet transition than for ER-to-ramjet transition. The major challenge of the IRS design is that combustion must occur in a large cross-section combustor at low ram Mach numbers. This requires even distribution of the fuel, which is hard to accomplish without the assistance of spray bars or other components that will obstruct the flowpath during other modes.

A scaled-down version of the GTX RBCC engine has been constructed and installed at the direct-connect facility at NASA John H. Glenn Research Center at Lewis Field. The model engine consists of a translating centerbody mounted on a flat plate and surrounded by a contoured cowl. Both the centerbody and cowl are semicircular in cross section. The forward section of the centerbody mimics the area ratio profile of the full-sized GTX engine design. A backward-facing step behind the centerbody's widest point provides an isolator region for fuel injection and mixing. A combustor section with a divergence half-angle of 5 deg is connected to the cowl. The rocket motor is located at the aft end of the centerbody, and the plume exhausts parallel to the flat plate. Two fuel injector banks are located in the isolator region. Each bank consists of 11 fuel injectors that are equally spaced around the circumference of the cowl. The injectors are all 0.2 in. (0.508 cm) in diameter. These fuel injectors allow for IRS operation of the engine. ER operation is accomplished by not injecting any fuel. More details of the test apparatus and experimental results obtained are given by Kamhawi et al.[3]

The present work focuses on simulating the flow within this model engine. The purpose of the computational fluid dynamics (CFD) work is to understand the flow and combustion physics during IRS and ER operation and in transition to pure ramjet mode. The CFD work began with an attempt to match experimental cold-flow data.[4] The work has progressed into simulation of ER and IRS operation.[5] A summary of cold-flow results and several ER and IRS cases are discussed in this paper.

Numerical Methods

The numerical solutions were produced using a validated Navier–Stokes flow solver for unsteady, reactive flow calculations on massively parallel architectures.[6–8] The solver incorporates high-resolution upwind differencing based on the low-diffusion, flux-splitting scheme of Edwards.[9] Time integration is accomplished using a dual-time-stepping procedure to maintain second-order temporal accuracy. This integration is done implicitly via incomplete block factorization and planar Gauss–Seidel relaxation in order to allow for time steps that are much larger than possible with an explicit integration scheme. Increased computational efficiency is achieved by storing the factorization of the system Jacobian matrix for each subdomain in physical memory. After an initialization period when the Jacobian must be calculated at each iteration, the frequency of Jacobian calculations is lowered, and the code is able to perform many more iterations in the same amount of CPU time. Communication between subdomains is accomplished via Message Passing Interface. Second-order spatial accuracy is achieved through minmod-limited MUSCL extrapolation of the variables to the faces of the control volumes.[10] Use of the minmod slope limiter reduces the accuracy to first order near discontinuities.

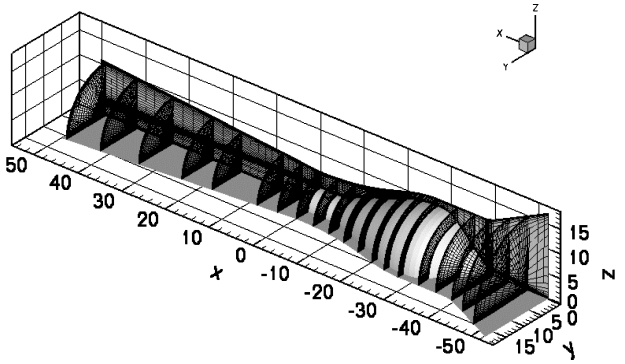

Fig. 2 Computational mesh used for ER and IRS simulations.

Hydrogen–air combustion is modeled using either Jachimowski's 7-species/7-reaction mechanism or Jachimowski's 9-species/18-reaction mechanism (see Refs. 11–13). The turbulence model used is Menter's hybrid k–ε/k–ω model.[14] The compressibility correction of Wilcox is also incorporated into the turbulence model.[15] Constant turbulent Prandtl and Schmidt numbers of 0.9 were assumed for all cases.

The solver has been validated for steady-state shock/hydrogen flame configurations as well as other cases.[6] The code has been validated for both two- and three-dimensional dynamic simulations of time-dependent hydrogen fuel injection in a scramjet inlet-combustor configuration.[7,8]

For the computational grid, half-plane symmetry with respect to the y axis is assumed. The physical domain for the $y > 0$ half of the engine is discretized using a mesh of 3.3 million points divided into 98 subdomains of equal size. Resolution of the fuel injectors is enhanced by tighter mesh spacing in the diffuser section. The diffuser section is connected to its upstream and downstream sections via a patched-grid interface. A picture of the grid is shown in Fig. 2. For one of the IRS cases, a coarse grid was used. The coarse grid was generated by removing every other point from the fine grid in the axial and radial directions.

Two different inlet boundary conditions were tried for the cold-flow and ER solutions: a constant mass flow boundary condition and a constant total pressure boundary condition. The constant mass flow boundary condition, which more closely represents the experimental setup, fixes $\dot{m}_i$, $T_{0,i}$, $Y_{s,i}$, and velocity direction (i.e., $\boldsymbol{v}/\|\boldsymbol{v}\|$) while extrapolating p from the interior. The constant total pressure boundary condition, which more closely represents flight conditions, fixes $p_{0,i}T_{0,i}$, $Y_{s,i}$, and $\boldsymbol{v}/\|\boldsymbol{v}\|$ while extrapolating u from the interior. Both of these boundary conditions yielded identical results for the cold-flow and ER solutions. However, for IRS solutions, the constant mass flow boundary condition could not be used because of the presence of the thermal throat. The location of the thermal throat dictates the mass flow rate through the combustor. For IRS cases, the constant total pressure boundary condition and a characteristic boundary condition were used, and they produced identical results. The characteristic boundary condition differed from the constant total pressure boundary condition in that the Riemann invariant $w_3 = u - 2a/\gamma$ was extrapolated rather than u.

The exit boundary condition was a mixed subsonic/supersonic boundary condition where all variables were extrapolated wherever $M > 1$. Where $M < 1$, p_e was fixed while u, v, w, T, and Y_s were extrapolated from the interior. At the solid walls, the adiabatic, no-slip boundary condition was applied:

$$u = v = w = \frac{\partial T}{\partial n} = \frac{\partial \rho_s}{\partial n} = 0$$

Table 1 Test case conditions

Test case	$p_{t,i}$	p_c	MR	ϕ	p_e
ESP 39	13.1 (90.3)	N/A	N/A	0.0	3.1 (21.4)
ESP 41	13.1 (90.3)	N/A	N/A	0.0	8.2 (56.5)
ER 8081	6.7 (46.2)	750 (5,171)	4	0.0	2.2 (15.2)
ER 8687	13.4 (92.4)	750 (5,171)	4	0.0	2.6 (17.9)
IRS NCSU 1500	32.0 (220.6)	1500 (10,342)	6	1.0	2.2 (15.2)
IRS NCSU 1000	32.0 (220.6)	1000 (6,895)	6	1.0	2.2 (15.2)
IRS NCSU 750	32.0 (220.6)	750 (5,171)	6	1.0	2.2 (15.2)

The rocket exit was modeled as a supersonic inflow plane to the combustor (i.e., Dirichlet boundary condition). The rocket exit conditions for each mass ratio and chamber pressure were calculated using the NASA Glenn program CEA (Chemical Equilibrium Applications).[16] The rocket was assumed to operate at 95% combustion efficiency. This was modeled in the CEA code by assuming that 5% of the hydrogen injected into the rocket plenum was inert and the other 95% was fully reactive.

Convergence of the numerical solutions was monitored by calculating the mass flow rate through five planes in the engine. When the relative error between the maximum and minimum of these five values was less than 0.1%, calculations were stopped. In addition to mass flow rate monitoring, the pressure profiles at the final iteration were compared with previous pressure profiles to ensure that the solution was no longer changing.

Test Cases

Two cold-flow test cases, two ER test cases, and three IRS test cases are presented in this work. The cold-flow and ER cases both correspond to tests completed in the direct-connect facility at NASA Glenn Research Center. The conditions for each of these cases are given in Table 1.

The symbols $p_{t,i}$, p_c, MR, ϕ, and p_e stand for the inlet total pressure, rocket chamber pressure, rocket mass ratio, equivalence ratio in the fuel–airstream, and rig exit pressure, respectively. All pressures are given in psia (kPa). The mass ratio is defined as the ratio of oxygen to hydrogen by mass (e.g., stoichiometric conditions would correspond to MR = 8).

The IRS cases constitute the first three stages of a five-stage, throttle-down process for the rocket. This purpose of this sequence of runs is to arrive at a chamber pressure of 400 psia (2758 kPa) while maintaining the thermal throat. The engines on the vehicle are expected to thermally choke while the rocket is running at a high chamber pressure (between 2000 and 1500 psia) (13,790 and 10,342 kPa). Initializing the rocket to a chamber pressure at less than 1500 psia (10,342 kPa) does not allow a thermal throat to form, but a solution with an existing thermal throat can be throttled down gradually so that the thermal throat is maintained. The chamber pressure of 400 psia (2758 kPa) corresponds to flight conditions at Mach 2.5, just prior to mode transition (i.e., rocket cutoff). Because the experimental rig cannot achieve a chamber pressure of 1500 psia (10,342 kPa), future IRS tests will not follow the flight trajectory conditions in order to induce thermal choking. Instead, the ratio of rocket chamber pressure to inlet total pressure will be set sufficiently high to induce thermal choking, subject to the constraints of the maximum rocket chamber pressure (i.e., the inlet total pressure will start off at a low value and then will be raised after a thermal throat is created).

Results for Cold-Flow Cases

The cold-flow results presented correspond to tests ESP 39 and ESP 41. Calculations for these cases were presented in a previous paper, but a geometry error led to significant discrepancies between the CFD predictions and the experimental data.[4] The geometry error was corrected, and then the calculations were repeated for the two cases.

Figures 3 and 4 compare the pressure predicted by the CFD calculations to the experimental results for case ESP 39 along the centerline and cowl 0-deg line, respectively. The term "centerline" refers to the intersection of the symmetry plane with the flat plate in the combustor section and the intersection of the symmetry plane with

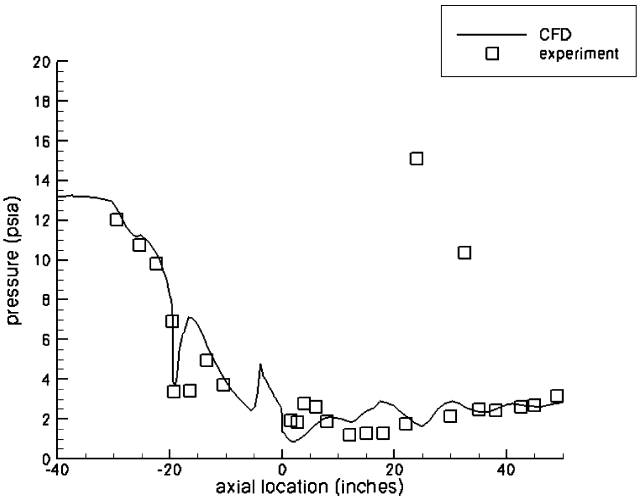

Fig. 3 Centerline pressure comparison for ESP 39.

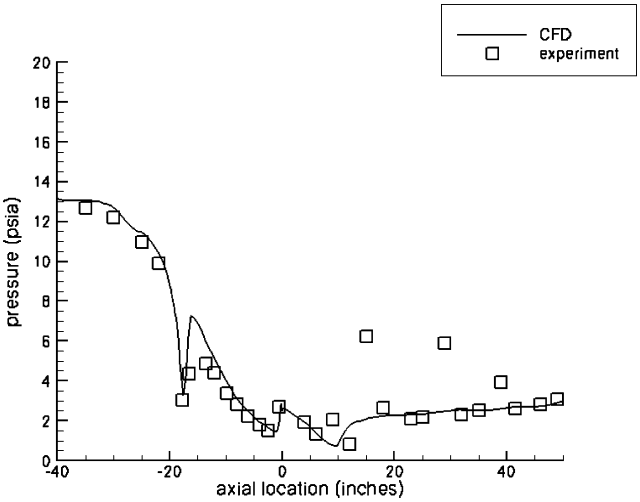

Fig. 4 Cowl pressure comparison for ESP 39.

the centerbody in the inlet and isolator sections. The term "cowl 0-deg line" refers to the intersection of the symmetry plane with the cowl. The backward-facing step along the centerbody is visible as a pressure rise at about $x = -20$ in. (−50.8 cm). The back of the centerbody is located at $x = 0$ in. For this case, there is good agreement between the predicted and measured cowl pressures along the entire length of the engine. However, there is a discrepancy in the centerline pressures between $x = 0$ and $x = 20$ in. (50.8 cm). This is the region just aft of the rocket exit. Because the rocket was covered with a plate for all of the cold-flow cases, it was modeled as a solid surface in the CFD calculations. The CFD calculations did not capture the pressure waves in this region as well as was desired. It is possible that the discrepancy is due to a lack of resolution (examined in detail for later cases), but it is also possible that the Reynolds averaged Navier–Stokes turbulence model may not accurately predict the turbulent wake behind the centerbody. However, this region was filled by the rocket plume (rather than a turbulent wake) for hot-flow tests, and so this particular problem was unique to this case.

Figures 5 and 6 compare the pressure from the CFD prediction to the experimental data for case ESP 41 along the centerline and cowl 0-deg line, respectively. For this case, there is good agreement between the predicted and measured pressures along both surfaces along the entire length of the engine. Because this case had a higher back pressure than case ESP 39, the flow at the exit was subsonic, and a large region of flow separation was present along the flat plate behind the rocket exit. Because the flow was separated at the combustor exit, 50 in. (127 cm) of the facility was added to the grid so that a well-posed outflow boundary condition could be enforced.

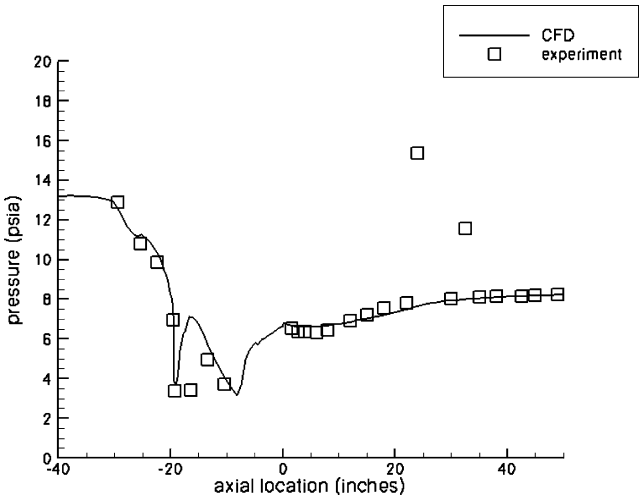

Fig. 5 Centerline pressure comparison for ESP 41.

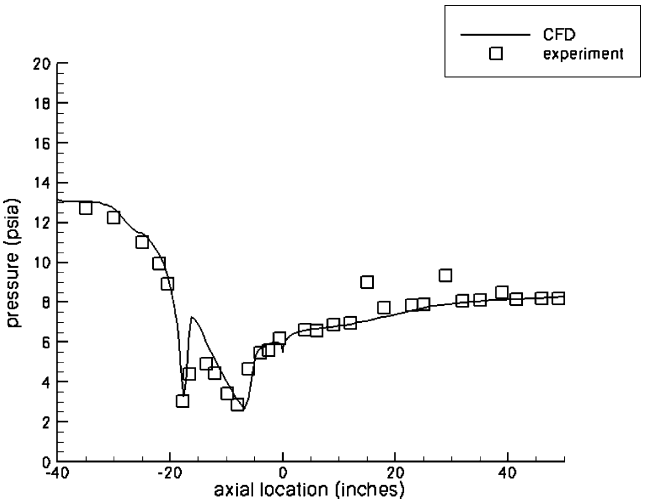

Fig. 6 Cowl pressure comparison for ESP 41.

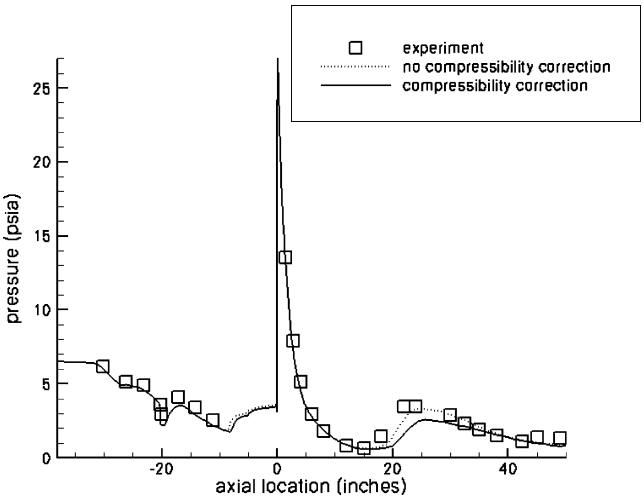

Fig. 7 ER 8081 centerline pressure with and without compressibility correction.

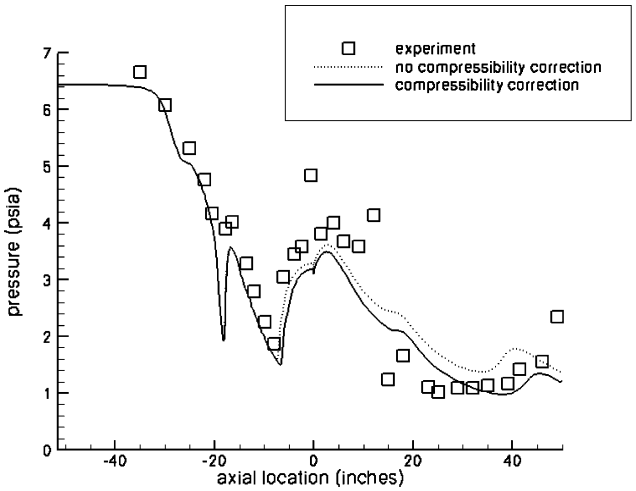

Fig. 8 ER 8081 cowl pressure with and without compressibility correction.

For this case, the back pressure at 100 in. (254 cm) was modified until the correct pressure at 50 in. (127 cm) (the end of the combustor) was matched.

Results for ER Cases

The ER results presented correspond to tests ER 8081 and ER 8687, two of the ER experiments completed to date. Figure 7 shows the centerline pressure predicted by two CFD calculations compared to the experimental data for ER 8081. Figure 8 shows the cowl pressures for the same case. One of the CFD calculations was performed with the compressibility correction, and the other was performed without the compressibility correction. Along the centerline and along the portion of the cowl upstream of the flame influence, the solution without the compressibility correction agrees better with the experimental data. However, along the portion of the cowl downstream of the flame influence, the solution with the compressibility correction agrees better with the experimental data. This is because the solution without the compressibility correction overpredicts the mixing. Because diffusion flames are mixing driven, the overprediction in mixing leads to higher heat release and thus higher wall pressures. Both of these solutions have an additional constraint of $u \geq 0$ imposed at the exit of the combustor section. This is because there is axial separation along the cowl, and the outflow boundary condition is ill-posed wherever $u < 0$. The constraint was added in lieu of a domain extension because of the extreme cost of extending the domain for a reacting solution. Also, the axial separation region for these cases was limited to the last few inches of the cowl surface, just before the diverging combustor section is connected to the straight exhaust duct. Figures 9 and 10 compare the seven- and nine-species reaction mechanisms along the centerline and cowl, respectively. Both of these solutions and those that follow use the Wilcox compressibility correction.[15] The nine-species mechanism provides marginally better agreement with the experimental data throughout the engine. The lower wall pressures for the seven-species case show that it is slightly underpredicting the heat release. A slight increase in ignition delay is also visible for the seven-species case.

Contour plots of Mach number and OH mass fraction are given in Figs. 11 and 12, respectively. Because this is a rocket-dominated case, the secondary flow actually chokes at around $x = 35$ in. (89 cm). Because the expansion of the rocket into the secondary flow is so extreme, this choking mechanism is due to both heat addition and area reduction in the secondary stream. The heat addition is due partially to the mixing of the hot rocket exhaust with the secondary flow and partially to the secondary combustion where the air and excess hydrogen mix. The resulting diffusion flame can be seen in Fig. 12.

Figure 13 shows the centerline pressure predicted by the CFD calculations compared to the experimental data for ER 8687. Figure 14 shows the cowl pressure for the same case. As expected for ER operation in a relatively short combustor (50 in.) (127 cm), the heat release is not enough to form a thermal throat. The results are in good agreement with the experiment except for discrepancies along the cowl in the latter half of the combustor section, where the influence of the combustion is most evident. The strong shock wave aft

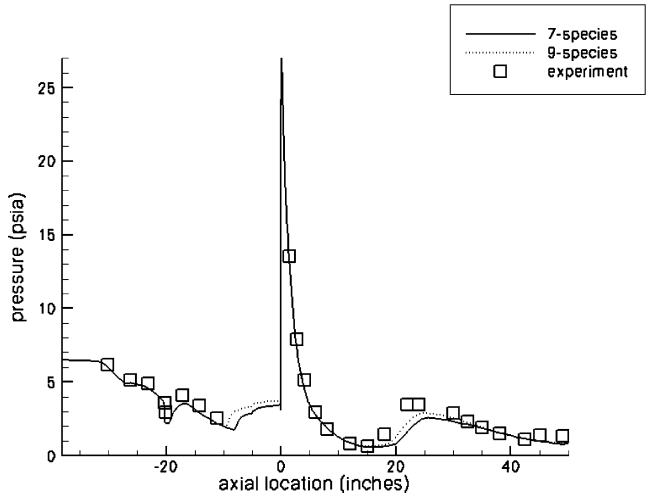

Fig. 9 ER 8081 centerline pressure with seven- and nine-species models.

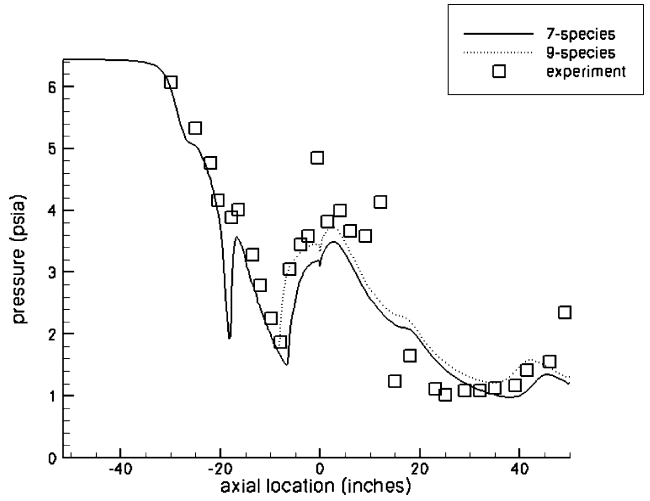

Fig. 10 ER 8081 cowl pressure from seven- and nine-species mechanisms.

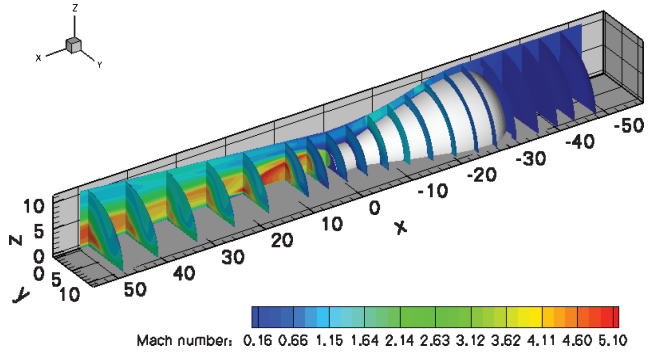

Fig. 11 Mach number contours for case ER 8081.

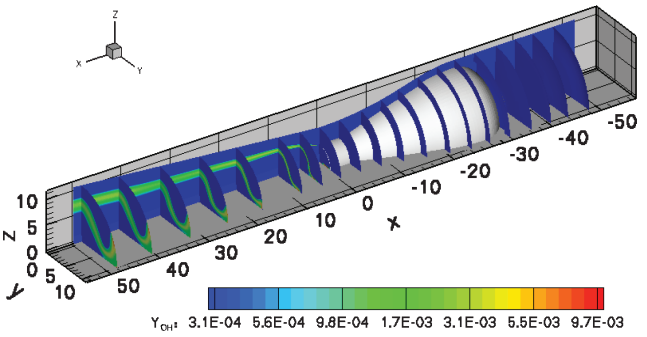

Fig. 12 OH mass fraction contours for case ER 8081.

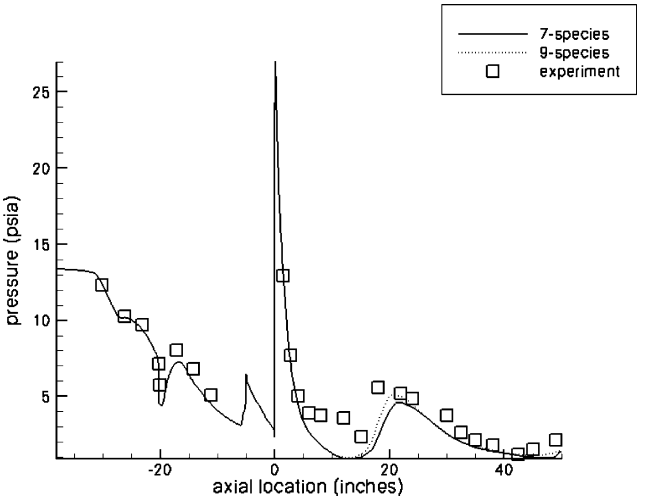

Fig. 13 Centerline pressures for case ER 8687.

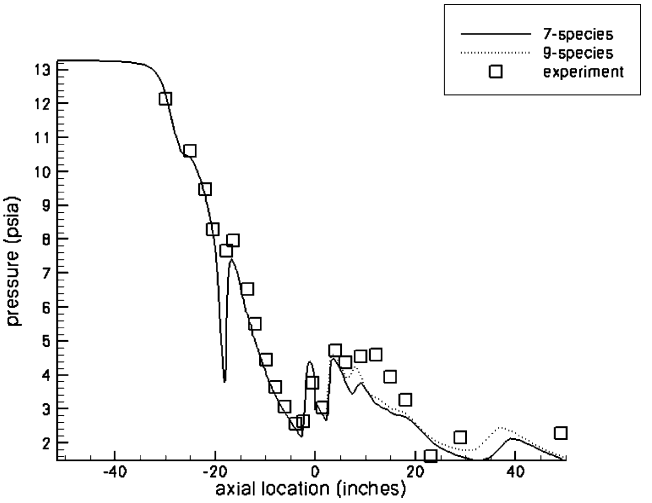

Fig. 14 Cowl pressures for case ER 8687.

of the rocket exit is caused by the impingement of the rocket plume upon the flat plate. A separation region follows this shock. The shock, separation, and reattachment are all predicted by the CFD solution; however, the shock-induced separation is much larger in the experimental data. It was again necessary to enforce $u \geq 0$ in order to keep the exit boundary condition well-posed. As was the case for ER 8081, the nine-species mechanism gives higher heat release and marginally better agreement with the experimental data than the seven-species mechanism.

Figure 15 shows the temperature contours for case ER 8687. Temperatures of around 4500°R are found in the flame front, whereas temperatures of around 5800°R are found where the rocket plume impinges on the flat plate. The rocket exhaust enters the combustion chamber at approximately 2630°R, and the additional fuel in the exhaust ignites almost immediately, forming a diffusion flame that is anchored at the rocket base plate and stretches the full length of the combustor. The flame front can be better seen in the contours of Y_{OH} in Fig. 16. Because significant amounts of OH are still present at the combustor exit, the combustion is incomplete.

Reaction Mechanism Comparison for IRS

Solutions for case IRS NCSU 750 were produced using both the seven- and nine-species reaction mechanisms. (Because no IRS

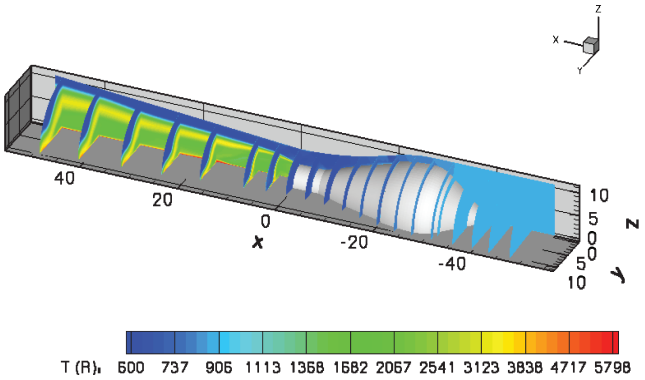

Fig. 15 Temperature contours for case ER 8687.

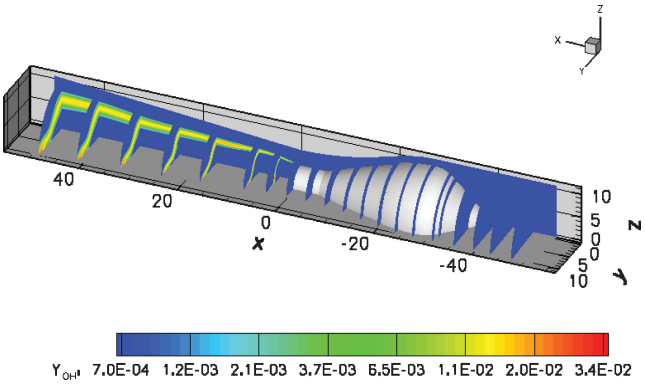

Fig. 16 OH mass fraction contours for case ER 8687.

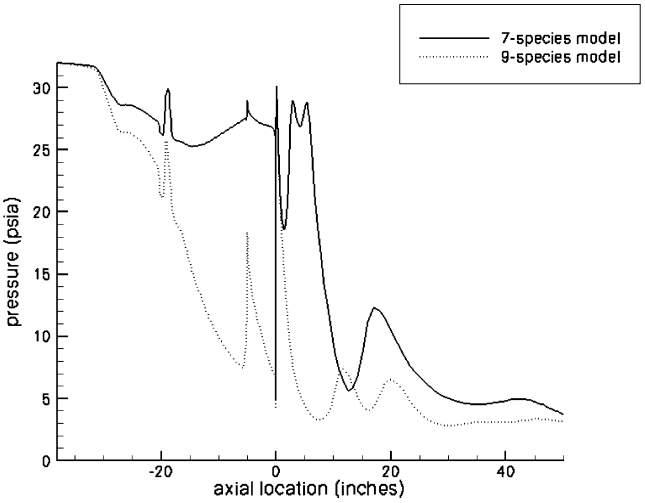

Fig. 17 Centerline pressure comparison for case IRS NCSU 750.

experiments have been completed to date, the cases designed at North Carolina State University contain "NCSU" in their naming convertion.) All of the fuel was injected through the upstream bank for this comparison. These solutions with $p_c = 750$ psia (5171 kPa) were produced using the $p_c = 1000$ psia (6895 kPa) solution for an initial condition, which was produced using the $p_c = 1500$ psia (10,342 kPa) case for an initial condition. The reason for this is that the calculation could not establish a thermal throat unless $p_c/p_{t,i}$ was high enough. The highest chamber pressure that can be replicated with the experimental apparatus is 750 psia (5171 kPa), so that case was chosen for the reaction mechanism comparison. This will allow CFD results to be compared with experimental IRS data once they become available.

Figures 17 and 18 show the centerline and cowl pressures, respectively, for both reaction mechanisms. The huge discrepancies in the

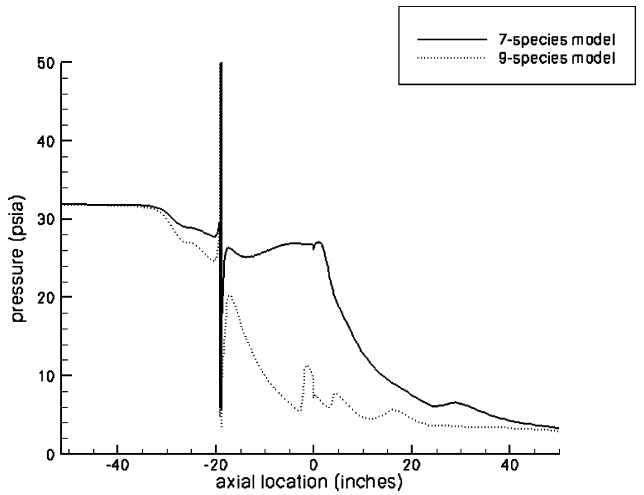

Fig. 18 Cowl pressure comparison for case IRS NCSU 750.

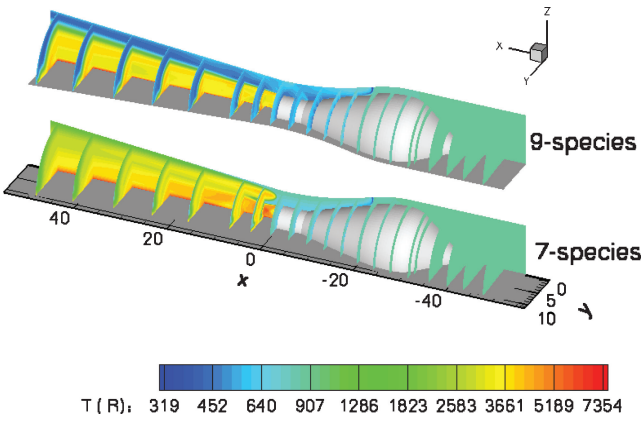

Fig. 19 Temperature contours for case IRS NCSU 750.

pressure profiles are present because the seven-species solution is thermally choked, whereas the nine-species solution is not. The large spike in the cowl pressure is present because the data series passes through one of the fuel injectors. Although the nine-species reaction mechanism resulted in slightly higher heat release for the ER test cases, it shows a much higher premixed ignition delay than the seven-species mechanism. Ignition delay is fairly insignificant for the mixing driven, diffusion flame present in ER operation (which is stabilized by the hot rocket exhaust), but it is very significant for the partially premixed flame structure present in IRS operation. The slower ignition and chain-branching kinetics predicted by the nine-species solution result in poor flame propagation and incomplete combustion in the secondary stream. Because less of the fuel–air mixture burns in the nine-species solution, the heat release is not enough to thermally choke the flow. Figure 19 shows the temperature contours for both the seven- and nine-species solutions. In addition to the difference in flame structure, the difference in isolator flow features can be seen in this plot. Because there is no thermal throat in the nine-species solution, the flow physically chokes just aft of the injectors, and a series of oblique shocks is induced by the sharp corner where the centerbody and rocket cowl meet. These features are not present in the seven-species solution because the flame and thermal-throat structure provide a high enough backpressure to keep the isolator flow subsonic. Figure 20 shows the detail of the flame structures using mass fraction contours for monatomic hydrogen. For the nine-species solution, there is a diffusion flame oriented along the mixing layer between the primary and secondary streams, but there is no premixed flame propagating out toward the cowl. For the seven-species solution, the premixed flame propagation is fast enough to result in the formation of a lifted, triple-flame structure in the partially premixed secondary stream. The triple point of the

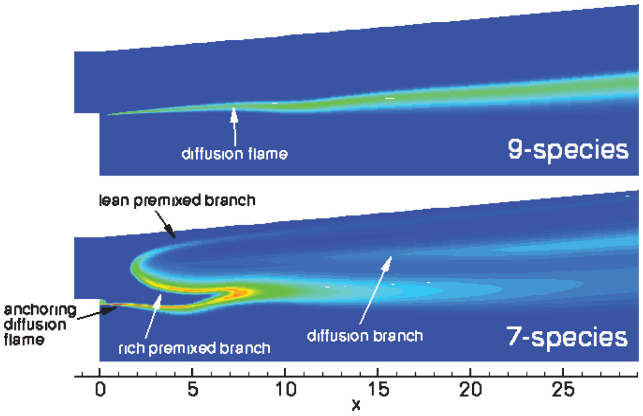

Fig. 20 Comparison of H mass fraction contours.

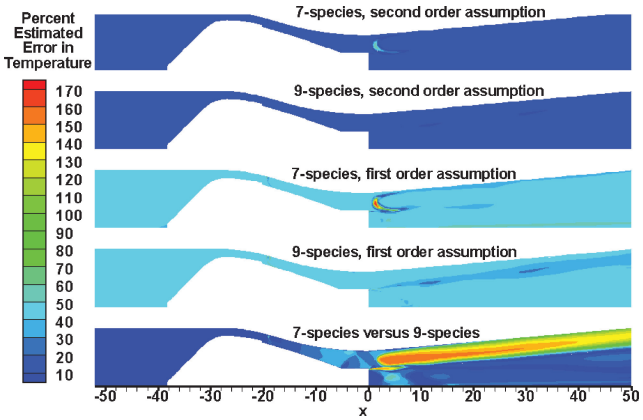

Fig. 21 Estimated discretization error for temperature.

lifted flame is in the vicinity of the stoichiometric line. Two premixed branches, one rich and one lean, propagate from this point. Behind the lean premixed branch, there is a surplus of oxidizer, and there is a surplus of fuel behind the lean branch. A diffusion-flame branch forms where these two regions meet.

Because it was known that the existence or nonexistence of a thermal throat was dependent on the initial conditions of a given simulation, the question of whether a thermally choked nine-species solution could be attained with different initial conditions needed to be addressed. To do this, a solution was obtained starting with the thermally choked seven-species solution as an initial condition. Another solution was obtained by freezing the thermal and kinetic variables while allowing the chemical compositions of HO_2 and H_2O_2 to "catch up" before the thermal and kinetic variables were allowed to evolve with time. Both sets of conditions converged to the unchoked solution.

Grid Resolution Study for IRS

Obtaining a solution on a coarsened mesh provides an indication for how far the fine solution is from grid converged. The $p_c = 750$ psi (5171 kPa) case was simulated on both the fine and coarse grids for both reaction mechanisms. An estimate of the discretization error for a generic variable ϕ is given by

$$E_{\text{fine}} = \frac{\phi_{\text{coarse}} - \phi_{\text{fine}}}{\phi_{\text{fine}}(r^p - 1)}$$

where r is the ratio of grid refinement and p is the order-of-accuracy of the scheme.[17] Figure 21 shows the estimated errors for both reaction mechanisms assuming both first- and second-order spatial convergence of the code and also gives the percent difference between the seven- and nine-species solutions for comparison (using the average of the two as the reference).

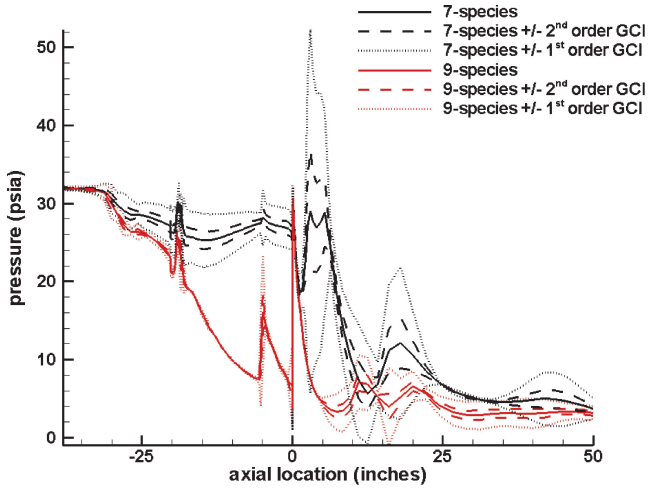

Fig. 22 GCI for centerline pressure.

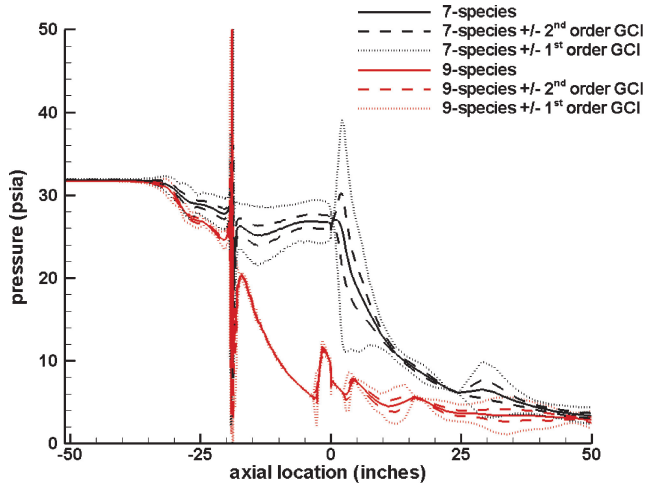

Fig. 23 GCI for cowl pressure.

A second-order assumption is aggressive in this case, even though the code is nominally second-order accurate. This is because a claim of second-order accuracy can be proved only by comparing three grid levels; the presence of shock waves activates the limiter, and error that is dependent on resolution in the circumferential direction does not show up in Fig. 21. A first-order assumption is more conservative, even though the true error is likely somewhere between the first- and second-order estimates. The estimated temperature error is helpful in determining the source and extent of discretization error related to the reaction models. It can be seen that the seven-species model contains significant discretization error related to the location of the flame front but far less discretization error related to the overall heat release. The high percent error in the vicinity of the flame front is because the coarse solution has the flame front farther forward than the fine solution, so that the reference temperature in the denominator is that of the unburned fuel–air mixture. Lower resolution raises the flame speed by increasing the amount of numerical mass and thermal diffusion. The nine-species solution contains little error in flame location or heat release relative to the differences between the two reaction mechanisms.

Another useful measure of discretization error is the grid convergence index (GCI), which is essentially a factor of safety of three multiplied by the estimated error. Because of the factor of safety, the GCI represents a confidence interval rather than simply an error estimate.[17] The centerline and cowl pressure GCI are plotted for both reaction mechanisms in Figs. 22 and 23, respectively. Because the conservative first-order confidence intervals overlap significantly for the centerline pressure behind the rocket, it can be said that the resolution in this region (i.e., in the region of shock

waves and shock-induced separation) is insufficient to support conclusions about the influence of the different reaction mechanisms there. However, the cowl pressure GCI bands are sufficiently separated that conclusions can be drawn and supported regarding differences in the prediction of premixed combustion in the secondary flow (i.e., in the region of the cowl rather than centerline data).

Reduced chemical kinetics rates in more complex reaction models are relatively common in high-speed propulsion applications. For example, in simulations of nonvitiated, supersonic, hydrogen–air combustion downstream of a ramped injector, Goyne et al. found the ignition kinetics of even the seven-species model to be too slow for proper flame stabilization, and so they reverted to a four-species/one-step model.[18,19] Increasingly complex chemistry models are proportionately more sensitive to Schmidt number effects, and advanced models that account for the effects of turbulent fluctuations on reaction rates have not yet been extensively validated for combustion at high Mach numbers. Future work will include a simplified temperature probability density function approach to account for the effects of temperature fluctuations on reaction rates and could reduce the ignition delay for the nine-species model,[5] but in the absence of experimental data for IRS operation, it is impossible to determine which approach (if any) best represents the physics.

Conclusions

This paper has described several numerical simulations of the GTX RBCC combustor in cold-flow, ejector-ramjet (ER), and independent ramjet stream (IRS) operation. The solutions for cold-flow conditions and ER conditions are in reasonable agreement with available experimental data, and IRS solutions have been obtained for two reaction mechanisms and two grid sizes. Although ER results indicate that the seven- and nine-species reaction models produce only slightly different solutions, IRS results show a much more dramatic impact. This is because of the dependence of premixed flame structures on ignition and chain-branching kinetics. IRS results also showed sensitivity to grid resolution, especially in the rocket plume where numerous shock waves are present.

Acknowledgments

The authors thank the North Carolina Supercomputing Center, which provided computational resources for this work, and NASA Glenn Research Center, which provided funding under Grant NAG3-2658. This work was sponsored by the Alternate Energy Foundation Technologies Subproject of the Low Emissions Alternative Power Project at the NASA Glenn Research Center. Sandia is a multiprogram laboratory operated by Sandia Corporation, a Lockheed Martin Company, for the United States Department of Energy's National Nuclear Security Administration under Contract DE-AC04-94AL85000.

References

[1]Trefny, C. J., "An Airbreathing Launch Vehicle Concept for Single Stage to Orbit," AIAA Paper 99-2730, June 1999.

[2]Steffen, C. J., and Yungster, S., "Computational Analysis of the Combustion Processes in an Axisymmetric, RBCC Flowpath," NASA TM 2001-210679, Feb. 2001.

[3]Kamhawi, H., Krivanek, T. M., Thomas, S. R., and Walker, J. F., "Direct-Connect Ejector Ramjet Combustor Experiment," AIAA Paper 2003-0016, Jan. 2003.

[4]Steffen, C. J., Bond, R. B., and Edwards, J. R., "Three Dimensional CFD Analysis of the GTX Combustor," JANNAF CS/APS/PSHS/MSS Joint Meeting, April 2002.

[5]Bond, R. B., and Edwards, J. R., "CFD Analysis of an Independently Fueled Ramjet Stream in an RBCC Engine," AIAA Paper 2003-0017, Jan. 2003.

[6]Roy, C. J., and Edwards, J. R., "Numerical Simulation of a Three-Dimensional Flame/Shock Wave Interaction," *AIAA Journal*, Vol. 38, No. 5, 2000, pp. 745–753.

[7]McDaniel, K. S., and Edwards, J. R., "Simulation of Thermal Choking in a Model Scramjet Combustor," AIAA Paper 99-3411, June 1999.

[8]McDaniel, K. S., and Edwards, J. R., "Three-Dimensional Simulation of Thermal Choking in a Model Scramjet Combustor," AIAA Paper 2001-0382, Jan. 2001.

[9]Edwards, J. R., "A Low-Diffusion Flux-Splitting Scheme for Navier–Stokes Calculations," *Computers and Fluids*, Vol. 26, No. 6, 1997, pp. 635–659.

[10]van Leer, B., "Towards the Ultimate Conservative Difference Scheme, V: A Second-Order Sequel to Godunov's Method," *Journal of Computational Physics*, Vol. 32, No. 1, 1979, pp. 101–136.

[11]Jachimowski, C. J., "An Analytical Study of the Hydrogen–Air Reaction Mechanism with Application to Scramjet Combustion," NASA TP-2791, Feb. 1988.

[12]Drummond, J. P., and Rogers, R. C., "A Numerical Model for Supersonic Reacting Mixing Layers," *Computer Methods in Applied Mechanics and Engineering*, Vol. 64, No. 1–3, 1987, pp. 39–60.

[13]Eklund, D. R., and Stouffer, S. D., "A Numerical and Experimental Study of a Supersonic Combustor Employing Swept Ramp Fuel Injectors," AIAA Paper 94-2819, June 1994.

[14]Menter, F. R., "Two-Equation Eddy-Viscosity Turbulence Models for Engineering Applications," *AIAA Journal*, Vol. 32, No. 8, 1994, pp. 1598–1605.

[15]Wilcox, D. C., "Progress in Hypersonic Turbulence Modeling," AIAA Paper 91-1785, 1991.

[16]McBride, B. J., and Gordon, S., "Computer Program for Calculation of Complex Chemical Equilibrium Compositions and Applications II: User's Manual and Program Description," NASA Reference Publ. 1311, June 1996.

[17]Roache, P. J., *Verification and Validation in Computational Science and Engineering*, Hermosa, Albuquerque, NM, 1998, pp. 114–136.

[18]Goyne, C. P., McDaniel, J. C., Rodriguez, C. G., Krauss, R. H., and McClinton, C. R., "Experimental and Numerical Study of a Dual-Mode Scramjet Combustor," AIAA Paper 2002-5216, 2002.

[19]Goyne, C. P., McDaniel, J. C., Quagliaroli, T. M., Krauss, R. H., and Day, S. W., "Dual-Mode Combustion of Hydrogen in a Mach 5, Continuous Flow Facility," *Journal of Propulsion and Power*, Vol. 17, No. 6, 2001, pp. 1313–1318.

S. Mahalingam
Associate Editor

Color reproductions courtesy of Sandia National Laboratories.